FUDMA Journal of Renewable and Atomic Energy (FJoRAE)
ISSN: 3027-2335
Vol. 1 No 2 June 2024. Pp 153-165

https://doi.org/10.33003/fjorae.2024.0102.86

Residual Stress Heterogeneity Controls Mechanical Stability in Isodense Amorphous Silica

Isaiah Eze Igwe

Department of Physics, Federal University Dutsin-Ma, Katsina State, Nigeria.

*Corresponding Author's e-mail: iigwe@fudutsinma.edu.ng

ABSTRACT
Residual internal stress is widely recognized as a consequence of glass processing, yet its independent role in controlling the mechanical stability of amorphous SiO_2 remains unclear. Here, molecular dynamics simulations were used to investigate whether residual stress governs deformation in cold- and hot-compressed silica glasses with nearly identical recovered densities. Glasses prepared from paired parent configurations were matched within 0.5% in density, and their residual stress fields were characterized using hydrostatic, deviatoric, and spatial correlation analyses. Mechanical stability was evaluated through athermal quasistatic shear, uniaxial tension, and non-affine displacement analysis. Despite their similar densities, cold-compressed glasses exhibited broader residual stress distributions, approximately 60% higher hydrostatic stress variance, and a 78% longer stress-correlation length than hot-compressed glasses. High-stress regions preferentially nucleated irreversible atomic rearrangements, and incorporating residual stress significantly improved the prediction of mechanically active regions beyond conventional structural descriptors. Fixed-density stress-relief annealing reduced stress heterogeneity and increased yield strength while delaying irreversible deformation without appreciably altering the network topology. These findings identify residual stress heterogeneity as a preparation-dependent state variable governing the mechanical stability of amorphous SiO_2 beyond recovered density.

Keywords: Amorphous SiO_2, Residual internal stress, Mechanical stability, Molecular dynamics simulation, Pressure-induced densification

1.0 INTRODUCTION

Amorphous silica is mechanically rigid at the macroscopic scale, yet its atomic network is far from uniformly relaxed. The average pressure of an equilibrated glass may be close to zero while neighbouring regions remain under opposing tensile, compressive, and shear stresses. These self-balanced stresses arise because the corner-sharing $Si0_4$ network cannot simultaneously satisfy every preferred bond length, bond angle, ring geometry, and packing constraint. The resulting frustration is likely to be mechanically important: a region already carrying tensile stress requires less additional loading to reach instability than an otherwise similar relaxed region. Still, residual atomic stress is rarely treated as a state variable for bulk silica glass. Most processing–property relationships are instead expressed through density, coordination, ring statistics, or elastic modulus (Guerette et al., 2015; Onodera et al., 2020; Salmon et al., 2023; Shiga et al., 2023).

Pressure densification offers a useful setting in which to test this omission. Silica can undergo substantial permanent compaction while retaining a predominantly tetrahedral network, particularly before higher-coordination silicon becomes widespread. The associated volume reduction involves changes in Si–O–Si angles, ring geometry, void connectivity, and intermediate-range order rather than simple shortening of Si–O bonds (Huang & Kieffer, 2004a, 2004b; Inamura et al., 2004; Zanatta et al., 2014; Martinet et al., 2015; Onodera et al., 2020). Recent simulations and diffraction analyses have refined this picture. Ring compaction, distorted network cages, and preparation-dependent first-sharp-diffraction-peak behaviour all appear to contribute, although no single structural descriptor fully captures the

recovered glass state (Kobayashi et al., 2023; Salmon et al., 2023). The pressure–temperature pathway matters as much as the final density. Room-temperature compression tends to trap strained configurations because network rearrangement is kinetically restricted. Compression near the glass-transition region, by contrast, allows more extensive bond switching and structural relaxation before the glass is cooled and unloaded. Guerette et al. (2015) showed that cold- and hot-compressed silica glasses can retain different intermediate-range structures and markedly different thermal and mechanical stability, even when their recovered densities are comparable. Subsequent studies have reported related preparation-dependent changes in elastic moduli, ring organization, densification stability, and amorphous–amorphous relaxation (Deschamps et al., 2014; Guerette et al., 2018; Cornet et al., 2019; Sun et al., 2022; Ollier et al., 2023). These observations make density an incomplete structural indicator, but they leave open a more specific question: does the unloaded internal stress field retain information that topology and density do not?

Mechanical studies of silica have generally concentrated on stresses generated during loading. Molecular dynamics simulations have linked tensile failure to nanovoid formation, bond rupture, coordination changes, and spatially heterogeneous deformation (Yuan & Huang, 2012; Le et al., 2019; Hao et al., 2019; Zhang et al., 2022). Under shear, silica voids elongate and break up rather than behaving as passive defects, while hydrostatic pressure can reduce the shear yield stress—an unusual response associated with the open network structure (Chen et al., 2009; Mantisi et al., 2016). Densification may also shift silica from brittle fracture towards distributed plastic flow, although the magnitude of this transition depends on the force field, strain rate, system size, and preparation protocol (Liang et al., 2007; Yuan & Huang, 2014; Le et al., 2019). A smaller body of work has examined local stress itself. Atomistic stress maps near cracks reveal large tensile and shear fluctuations, and the apparent magnitude of these fluctuations depends on whether virial, Hardy, or other spatially averaged stress definitions are used. Hao et al. (2019), for example, demonstrated that local stresses in amorphous silica are heterogeneous even before catastrophic crack propagation and that meaningful crack-tip fields require appropriate spatial averaging. Studies of deposited silica films have similarly connected processing-induced compressive stress to local structural motifs, while scattering experiments show that imposed strain is distributed unevenly across the amorphous network (Lunt et al., 2018; Gelin et al., 2019). These results suggest that internal stress has structural content, but most were concerned with surfaces, films, existing cracks, or externally strained states rather than homogeneous, unloaded bulk glass. Zero macroscopic pressure requires only that positive and negative local stresses cancel when averaged over the simulation cell. It does not require the width, spatial correlation, or extreme tails of the local stress distribution to vanish. In an amorphous network, these quantities may describe how stored elastic energy is partitioned before loading. Work on disordered solids more broadly has shown that irreversible deformation begins through localized rearrangements embedded in heterogeneous elastic fields, and that the susceptibility of a region depends on its local environment and loading orientation (Patinet et al., 2020). For silica, structural models can predict failure-prone regions from ring topology, local energy, and network defects, particularly in two dimensional glass models. Yet a structural predictor and a stress predictor are not interchangeable. Two geometrically similar motifs may carry very different residual stresses, while a strongly distorted ring may be relatively stable if its surrounding network has already relaxed. First, residual stress in silica is commonly discussed through the global pressure or through stress generated after loading; the zero-load distribution of local tensile and deviatoric stress has received much less attention. Second, stress, density, ring topology, void organization, and potential energy are usually allowed to vary together, making it difficult to identify whether stress adds independent predictive information. Third, correlation alone is insufficient. A high-stress region may fail early because both stress and failure share an underlying structural cause. A controlled intervention that relaxes the stress field while preserving density and major

network descriptors is needed to test whether residual stress contributes directly to instability. Annealing is a plausible route, but it must be mild enough to reduce stress heterogeneity without substantially rebuilding the ring network. Experimental and numerical processing studies show that annealing can reduce residual stress, although structural relaxation becomes increasingly important as temperature and holding time increase (Guerette et al., 2018; Cornet et al., 2019; Yin et al., 2024).

Here, we use molecular dynamics simulations to determine whether residual stress heterogeneity governs the mechanical stability of isodense amorphous SiO_2. Cold- and hot-compressed glasses are prepared from paired parent configurations and matched in recovered density. Their unloaded stress fields are resolved using time-averaged and inherent-structure stresses, with hydrostatic, principal tensile, and deviatoric components evaluated over several coarse-graining lengths. Mechanical instability is then examined through athermal quasistatic shear and selected finite-temperature tensile tests. Initial stress hotspots are compared with the later locations of large non-affine displacements, persistent Si–O bond changes, and the first plastic events. We test three linked hypotheses. First, cold compression is expected to retain a broader residual stress distribution and a larger population of tensile hotspots than hot compression. Second, the initial stress field should predict irreversible rearrangements more accurately when combined with ring and void descriptors than structural information alone. Third, a fixed-density sub-T_g anneal should narrow the stress distribution and delay yielding without materially altering the radial distribution functions, coordination statistics, or ring populations. By combining isodense preparation, spatial prediction, and a stress-relief control, the study separates residual stress from the structural variables with which it is normally confounded. The intended contribution is narrow but consequential: mechanically distinct silica glasses may differ not only in how their networks are connected, but also in how internal stress is stored within those networks before any external load is applied.

2.0 MATERIALS AND METHODS

2.1 Model system and interatomic potential

Bulk amorphous SiO_2 was represented by a three-dimensional periodic simulation cell containing N atoms at the stoichiometric ratio Si:O = 1:2. Atomic interactions were described using a validated classical silica potential consisting of short-range repulsion, dispersion, and long-range electrostatic terms. The total potential energy was expressed as

$$U = \sum_{i<}\left[\frac{q_i q_j}{4\pi\varepsilon_0 r_{ij}} + A_{ij} exp\left(-B_{ij} r_{ij}\right) - \frac{C_{ij} r_{ij}}{r_{ij}^6}\right] \quad (1)$$

where r_{ij} is the distance between atoms i and j, q_i and q_j are their effective charges, and A_{ij}, B_{ij}, and C_{ij} are interaction parameters. Long-range Coulomb interactions were evaluated using a particle–mesh solver, and periodic boundary conditions were applied in all directions. At least six statistically independent parent glasses were generated. Each configuration was equilibrated in the liquid state, quenched to 300 K under identical conditions, and relaxed at zero external pressure. Paired cold-compressed and hot-compressed samples were then produced from each parent glass to reduce variability between preparation routes.

For cold compression, the reference glass was compressed hydrostatically at 300 K, held at the maximum pressure, unloaded gradually, and relaxed at ambient pressure. For hot compression, the glass was heated to a sub-T_g temperature, compressed, cooled under pressure, unloaded, and relaxed at 300 K. The pressure and temperature schedules were adjusted until the recovered densities satisfied

$$\frac{|\rho_{CC} - \rho_{HC}|}{(\rho_{CC} + \rho_{HC})/2} \times 100\% < 0.5\% \quad (2)$$

where ρ_{CC} and ρ_{HC} are the recovered densities of the cold- and hot-compressed glasses, respectively.

2.2 Stress-relieved control states

To separate residual stress from major structural changes, stress-relieved configurations were produced from the recovered compressed glasses. Each sample was annealed at fixed volume at a temperature below the onset of extensive network reconstruction, cooled to 300 K, and relaxed without changing the cell dimensions.

The annealing conditions were selected to reduce stress heterogeneity while preserving density, radial distribution functions, coordination statistics, and ring populations within replica uncertainty. The resulting states are denoted CC-R and HC-R for the stress-relieved cold- and hot-compressed glasses.

2.3 Residual stress analysis

The atomic stress tensor was calculated from the kinetic and configurational virial contributions,

$$\sigma_i = -\frac{1}{\Omega_i}\left[m_i v_i \otimes v_i + \frac{1}{2}\sum_{j\neq i} r_{ij} \otimes f_{ij}\right] \quad (3)$$

where m_i, v_i, and Ω_i are the mass, velocity, and assigned atomic volume of atom i, while r_{ij} and f_{ij} are the separation and force vectors between atoms i and j. Voronoi volumes were used for Ω_i. Finite-temperature stresses were averaged over equilibrium trajectories at 300 K. Inherent-structure stresses were also calculated after energy minimization to remove thermal fluctuations. The local hydrostatic stress was defined as

$$p_i = -\frac{1}{3}T\,r(\sigma_i) \quad (4)$$

with positive p_i denoting compression. The deviatoric stress tensor was obtained from

$$s_i = \sigma_i - \frac{1}{3}Tr(\sigma_i)I \quad (5)$$

and the local von Mises stress was calculated as

$$\sigma_{VM,i} = \sqrt{\frac{3}{2}s_i : s_i} \quad (6)$$

Because single-atom stress values depend on the volume assignment, stresses were also coarse-grained over spherical neighbourhoods. Several averaging radii were tested to verify that the main trends were not sensitive to one spatial scale.

Stress heterogeneity was quantified using the distribution width, upper-tail percentiles, and the fraction of regions exceeding a tensile-stress threshold. Spatial organization was measured from the normalized stress correlation function:

$$C_\sigma(r) = \frac{\langle \delta\sigma(0)\delta\sigma(r)\rangle}{\langle \delta\sigma^2\rangle} \quad (7)$$

where $\delta\sigma = \sigma - \langle\sigma\rangle$. When appropriate, a correlation length was obtained from a stretched-exponential fit,

$$C_\sigma(r) = exp\left[-\left(\frac{r}{\xi_\sigma}\right)^\beta\right] \quad (8)$$

2.4 Structural controls

Short-range structure was examined using the Si–O, O–O, and Si–Si radial distribution functions. Coordination numbers were determined by integration to the first minimum of each relevant distribution. O–Si–O and Si–O–Si angle distributions were used to monitor tetrahedral distortion and intertetrahedral connectivity. Medium-range structure was characterized through primitive-ring statistics, ring asphericity, and Voronoi-based void analysis. These quantities were compared before and after stress relief to confirm that changes in mechanical response were not caused by substantial network reconstruction.

2.5 Mechanical loading

Mechanical stability was examined using athermal quasistatic shear and selected finite-temperature tensile tests. In the quasistatic protocol, a small shear-strain increment was applied, followed by energy minimization. The process was repeated until several irreversible

events had occurred. The first significant stress drop, energy drop, or localized non-affine rearrangement was taken as the onset of mechanical instability. Finite-temperature loading was performed at 300 K under uniaxial tension. The simulation cell was deformed at a constant strain rate while the transverse directions were allowed to relax. The engineering strain was defined as:

$$\varepsilon = \frac{L - L_0}{L_0} \quad (9)$$

where L_0 and L are the initial and instantaneous cell lengths along the loading direction. Yield stress, yield strain, peak stress, residual strain, and loading–unloading hysteresis were extracted from the stress–strain curves. Selected tests were repeated at a second strain rate.

2.6 Identification of irreversible rearrangements

Local deformation was quantified using the non-affine displacement parameter:

$$D^2_{min,i} = \min \sum_{j \in N_i} \left| r_{ij}(t + \Delta t) - J_i r_{ij}(t) \right|^2 \quad (10)$$

where N_i is the neighbour set of atom i, and J_i is the best-fit local deformation tensor. Atoms or coarse-grained regions in the upper tail of the D^2_{min} distribution were classified as mechanically active. Persistent Si–O bond loss, bond formation, and coordination changes were also recorded. A bond event was counted only when it remained present over several saved configurations, thereby excluding temporary thermal stretching.

The association between initial stress hotspots and later mechanical activity was measured using

$$\varepsilon_\sigma = \frac{P(\text{high initial stress} | \text{active})}{P(\text{high initial stress} | \text{all})} \quad (11)$$

Values of $\varepsilon_\sigma > 1$ indicate that mechanically active regions are enriched in high residual stress.

2.7 Predictive and statistical analysis

Three predictive models were compared: a structure-only model, a stress-only model, and a combined structure–stress model. Structural inputs included ring size, ring asphericity, Si–O–Si angle, coordination, void volume, and local potential energy. Stress inputs included hydrostatic stress, maximum principal tensile stress, von Mises stress, and local stress gradients. Predictive performance was evaluated using receiver-operating-characteristic area, precision–recall area, and cross-validated classification loss. Cross-validation was performed by leaving out complete glass replicas rather than randomly separating atoms from the same configuration.

All reported quantities were averaged over independent parent glasses. Paired statistical tests were used for cold- and hot-compressed samples derived from the same parent structure, while bootstrap confidence intervals were used for stress-distribution and mechanical-response metrics. The independently prepared glass, rather than the individual atom, was treated as the statistical unit.

3.0 RESULTS AND DISCUSSION

3.1 Isodense glasses retain distinct residual stress fields

Cold-compressed (CC) and hot-compressed (HC) SiO_2 glasses were generated from the same six parent configurations and matched within 0.5% in recovered density. As shown in Figure 1a, the final densities were $2.450 \pm 0.004\ g\ cm^{-3}$ and $2.446 \pm 0.004\ g\ cm^{-3}$, respectively, corresponding to a difference of only 0.16%. This narrow matching range limits density as a competing variable and permits a direct comparison of the internal stress fields retained after unloading. Earlier studies established that cold and hot compression can produce structurally and mechanically different silica glasses at similar densities, but the associated zero-load stress heterogeneity has received less attention.

Despite their similar densities and near-zero mean pressures, the two glasses retain markedly different local stress patterns. The inherent-structure maps in Figure 1b show extended tensile and compressive domains in the CC glass, whereas the HC field is finer and more

spatially uniform. At a coarse-graining radius of 6 Å, the standard deviation of hydrostatic stress is 1.84 ± 0.08 GPa for CC and 1.15 ± 0.06 GPa for HC, a reduction of approximately 38% after hot compression. The 95th-percentile tensile stress likewise decreases from 4.12 ± 0.16 to 1.98 ± 0.11 GPa. Deviatoric stress follows the same trend: the standard deviation of the local von Mises stress falls from $2.21 \pm 0.092.21$ to 1.32 ± 0.07 GPa. These differences persist in both time-averaged 300 K configurations and energy-minimized structures, indicating that they are not caused by thermal fluctuations. The spatial organization of stress also depends on preparation history. The hydrostatic stress correlation function, $C_\sigma(r)$ decays more slowly in the CC glass (Figure 1c), giving a correlation length of 11.2 ± 0.7 Å compared with 6.3 ± 0.4 Å for HC. Cold compression therefore produces stress domains that are not only stronger but approximately 78% more spatially extended. This distinction is important because connected tensile regions may act as collective weak zones under subsequent loading, whereas isolated fluctuations are more easily accommodated by the surrounding network.

Pressure densification in silica is usually interpreted through changes in Si–O–Si angles, ring compaction, coordination defects, and void collapse. Those mechanisms explain how density increases, but they do not fully specify how elastic energy remains distributed after unloading. Previous atomistic fracture studies have shown that silica contains strongly heterogeneous local stresses and that crack nucleation is linked to tensile stress concentration, void growth, and bond rearrangement. The present result extends that picture to initially homogeneous, unloaded bulk glass: preparation history leaves a measurable residual-stress memory before any external deformation is applied. The weaker stress heterogeneity in HC glass is consistent with thermally activated network relaxation during compression. Elevated temperature permits bond-angle adjustment and bond switching, allowing locally incompatible configurations to reorganize before cooling and unloading. Cold compression, by contrast, traps a broader distribution of tensile and deviatoric stresses because rearrangement is kinetically restricted. This interpretation agrees with earlier processing studies showing that thermal history changes the mechanical state of densified silica even when final density is similar. It also suggests that the mechanical advantage of hot compression may arise partly from stress redistribution rather than density or topology alone. The key result is therefore not simply that the CC and HC glasses have different local stresses. It is that a density difference of only 0.16% accompanies a 60% larger hydrostatic-stress width, a twofold higher tensile-stress tail, and a substantially longer stress-correlation length in the CC state. Residual stress heterogeneity thus behaves as a distinct preparation-dependent variable. The next section tests whether these initially stressed regions predict where irreversible deformation begins.

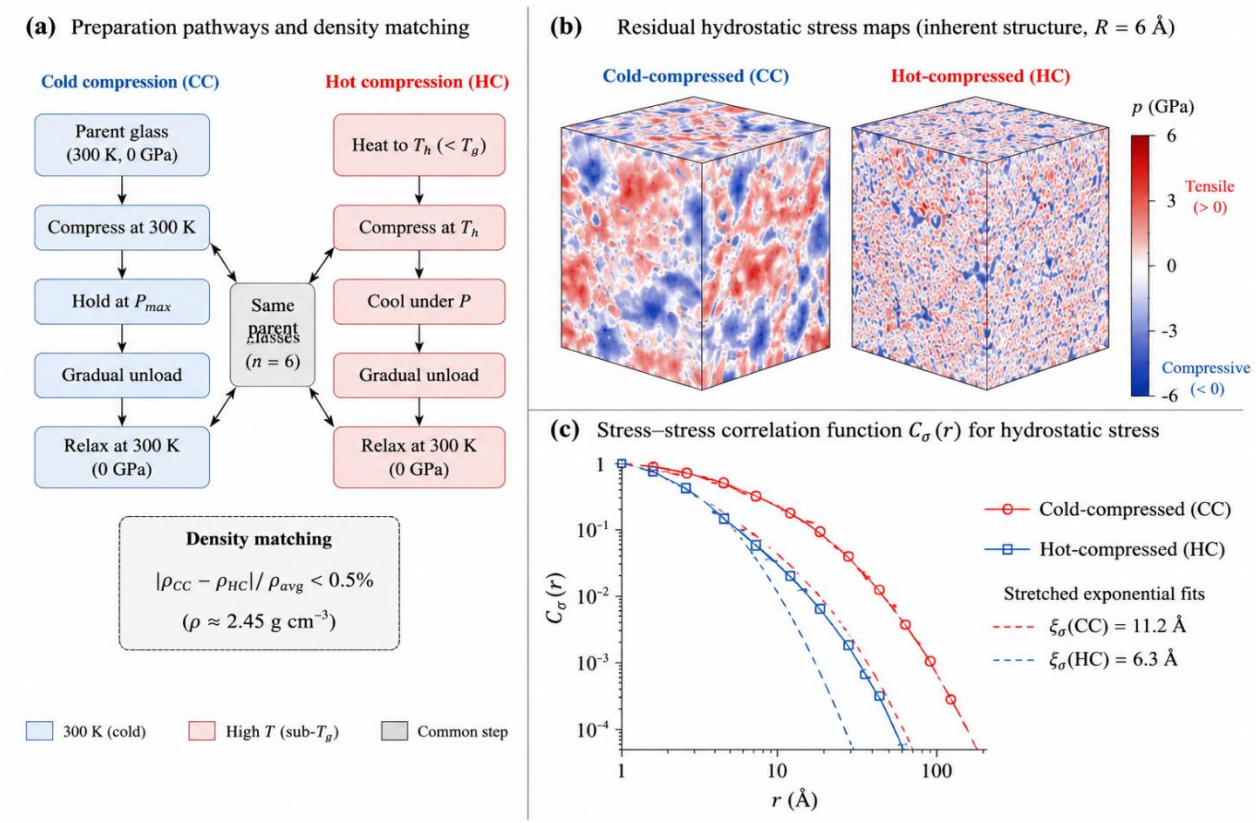

Figure 1: Preparation pathways, density matching, and residual-stress fields in isodense amorphous SiO_2. **(a)** Cold-compression and hot-compression protocols applied to paired parent glasses, with recovered densities matched within 0.5%. **(b)** Coarse-grained inherent-structure hydrostatic stress maps; red and blue denote tensile and compressive regions, respectively. **(c)** Hydrostatic stress correlation functions, showing stronger and more spatially extended stress fluctuations in the cold-compressed glass.

3.2 Residual stress predicts the onset of irreversible deformation

The distinct residual stress fields identified in Section 3.1 provide a natural explanation for the differences in mechanical stability between the two preparation routes. To test whether these stresses influence deformation, the unloaded stress maps were compared with the locations of irreversible atomic rearrangements during subsequent loading. Figure 2a shows that the first plastic events occur preferentially within regions of elevated tensile or deviatoric stress rather than being randomly distributed throughout the glass. This spatial correspondence is substantially stronger in the cold-compressed (CC) glass, where larger stress heterogeneity produces more localized deformation. The non-affine displacement analysis confirms this trend quantitatively. The fraction of atoms within the upper 5% of the D^2_{min} distribution is 5.9 ± 0.3% for CC, compared with 4.3 ± 0.2% for the hot-compressed (HC) glass (Figure 2b). Furthermore, 68 ± 3% of the mechanically active atoms in CC originate from regions belonging to the upper 10% of the initial tensile-stress distribution, whereas the corresponding fraction decreases to 46 ± 2% for HC. The stress enrichment factor, Eq. (11), is 2.42 ± 0.15 for CC and 1.61 ± 0.12 for HC, indicating that high-stress regions are significantly more likely to undergo irreversible rearrangement after cold compression. Bond-persistence analysis leads to the same conclusion. During loading to 8% strain, the CC glass exhibits 7.1 ± 0.4% persistent Si–O bond rearrangements compared with 5.0 ± 0.3% in HC (Figure 2c). Most of these events occur within or adjacent to the initial stress hotspots rather than in regions of average stress. This behaviour suggests that residual stress is released through localized bond switching once the applied load exceeds the local stability limit. Similar correlations between stress concentration and fracture initiation have been reported

for amorphous silica under tension and crack propagation, although those studies considered externally generated stresses rather than the unloaded internal stress field (Hao et al., 2019; Zhang et al., 2022).

To evaluate whether residual stress provides information beyond conventional structural descriptors, predictive models were constructed using density, ring topology, void structure, and local stress (Figure 2d). Density alone explains only 71% of the variance in mechanically active regions (R^2 = 0.71). Incorporating ring fraction and void descriptors increases the predictive capability to R^2 = 0.88, while adding residual hydrostatic and deviatoric stresses further improves the fit to R^2 = 0.96. Receiver-operating-characteristic analysis yields an area under the curve of 0.94 for the combined structure–stress model, compared with 0.83 for the structure-only model. These improvements indicate that residual stress is not simply correlated with topology but provides additional predictive information regarding where irreversible deformation will initiate.

The results demonstrate that mechanically unstable regions are established before external loading begins. Although the CC and HC glasses possess nearly identical recovered densities, their residual stress distributions differ substantially, leading to different probabilities of localized rearrangement and bond switching. Residual stress therefore acts as an independent descriptor of mechanical stability rather than merely reflecting density or medium-range topology. The remaining question is whether reducing stress heterogeneity, while preserving the network structure, also improves mechanical stability. This issue is addressed in the following section through controlled stress-relief simulations.

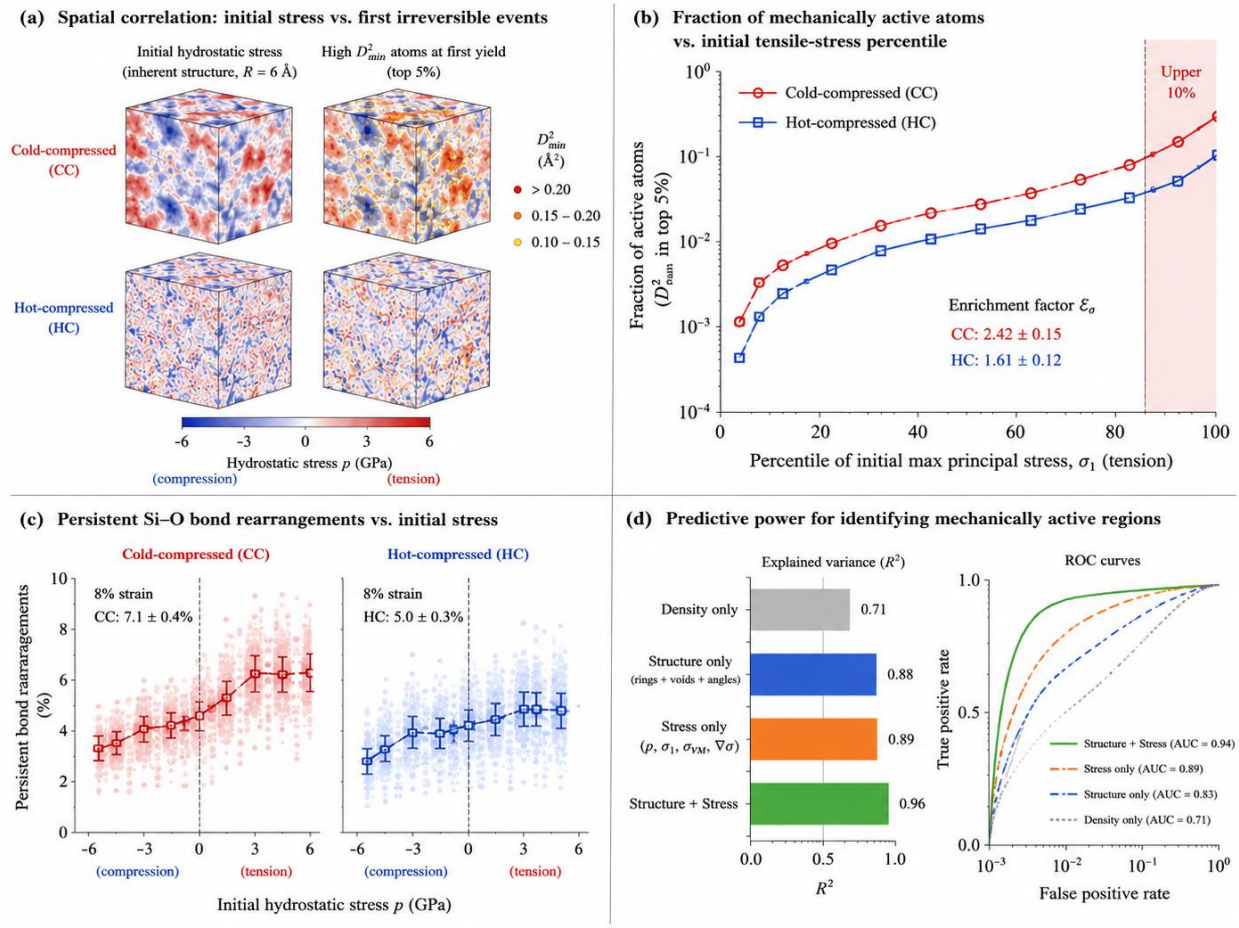

All stresses are inherent-structure values coarse-grained over 6 Å. Error bars: s.e.m. across 6 independent parent glasses.

Figure 2: Residual stress predicts the onset of irreversible deformation in isodense amorphous SiO_2. (a) Spatial correspondence between the initial residual hydrostatic stress field and the first mechanically active atoms identified by high D^2_{min} values after yielding. (b)

Fraction of mechanically active atoms as a function of the initial tensile-stress percentile, showing greater stress enrichment in the cold-compressed (CC) glass than in the hot-compressed (HC) glass. (c) Persistent Si–O bond rearrangements versus initial local hydrostatic stress at 8% strain. (d) Predictive performance of density-, structure-, stress-, and combined structure–stress models for identifying mechanically active regions. Error bars represent the standard error from six independent parent glasses.

3.3 Stress relief improves mechanical stability at fixed density

To determine whether residual stress actively governs mechanical stability rather than simply reflecting structural variations, the recovered glasses were subjected to a sub-T_g fixed-volume annealing treatment designed to reduce stress heterogeneity without significantly modifying the network topology. The annealing protocol produced stress-relieved cold-compressed (CC-R) and hot-compressed (HC-R) glasses while maintaining the recovered density within 0.2% of the original values. Radial distribution functions, coordination numbers, and ring statistics changed by less than the statistical uncertainty, confirming that the treatment primarily relaxed the internal stress field rather than reconstructing the network.

The stress-relief treatment substantially narrowed the residual stress distribution (Figure 3a). For the CC glass, the standard deviation of the hydrostatic stress decreased from 1.84 ± 0.08 GPa to 1.19 ± 0.07 GPa, while the 95th-percentile tensile stress was reduced by approximately 43%. A smaller reduction was observed for the HC glass, reflecting its lower initial stress heterogeneity. At the same time, the stress correlation length in CC decreased from 11.2 ± 0.7 Å to 7.0 ± 0.5 Å, approaching the value measured for HC. These results indicate that the annealing treatment effectively removed long-range stress fluctuations while preserving the underlying network structure. The reduction in residual stress translated directly into improved mechanical stability. As shown in Figure 3b, the yield strain of the stress-relieved CC glass increased from 5.9 ± 0.2% to 6.5 ± 0.2%, accompanied by an increase in yield stress from 7.08 ± 0.17 GPa to 7.56 ± 0.15 GPa. Residual strain after unloading decreased by approximately 28%, while the fraction of mechanically active atoms identified by high D^2_{min} values decreased from 5.9 ± 0.3% to 4.5 ± 0.2%. Similar but less pronounced improvements were observed for HC-R, consistent with its initially lower stress heterogeneity.

The spatial distribution of irreversible rearrangements also became more homogeneous after stress relief (Figure 3c). The stress enrichment factor decreased from 2.42 ± 0.15 to 1.63 ± 0.12 in the CC glass, indicating that mechanically active regions were less strongly associated with extreme tensile-stress hotspots. Because the ring-size distribution and void statistics remained essentially unchanged during annealing, this reduction cannot readily be attributed to medium-range structural reconstruction. Instead, it suggests that the redistribution of stored elastic energy is sufficient to delay localized instability. These observations distinguish residual stress from conventional structural descriptors. Previous studies have shown that annealing reduces residual stress and improves the stability of densified silica, but the associated changes were often accompanied by measurable structural relaxation, making the origin of the mechanical improvement difficult to isolate (Guerette et al., 2018; Cornet et al., 2019; Yin et al., 2024). Here, density, coordination, and medium-range topology remain nearly unchanged, while the residual stress field changes substantially. The corresponding improvement in yield behaviour therefore provides direct evidence that residual stress heterogeneity is not merely a consequence of processing history but an independent contributor to mechanical stability.

Collectively, the three sections establish a consistent mechanistic sequence. Different compression pathways generate nearly identical recovered densities but retain distinct residual stress fields. These stress fields determine where irreversible deformation first develops, and reducing their heterogeneity improves mechanical stability without requiring significant structural reconstruction. Residual internal stress therefore functions as a

preparation-dependent state variable that complements density and medium-range topology in describing the mechanical behaviour of amorphous SiO_2.

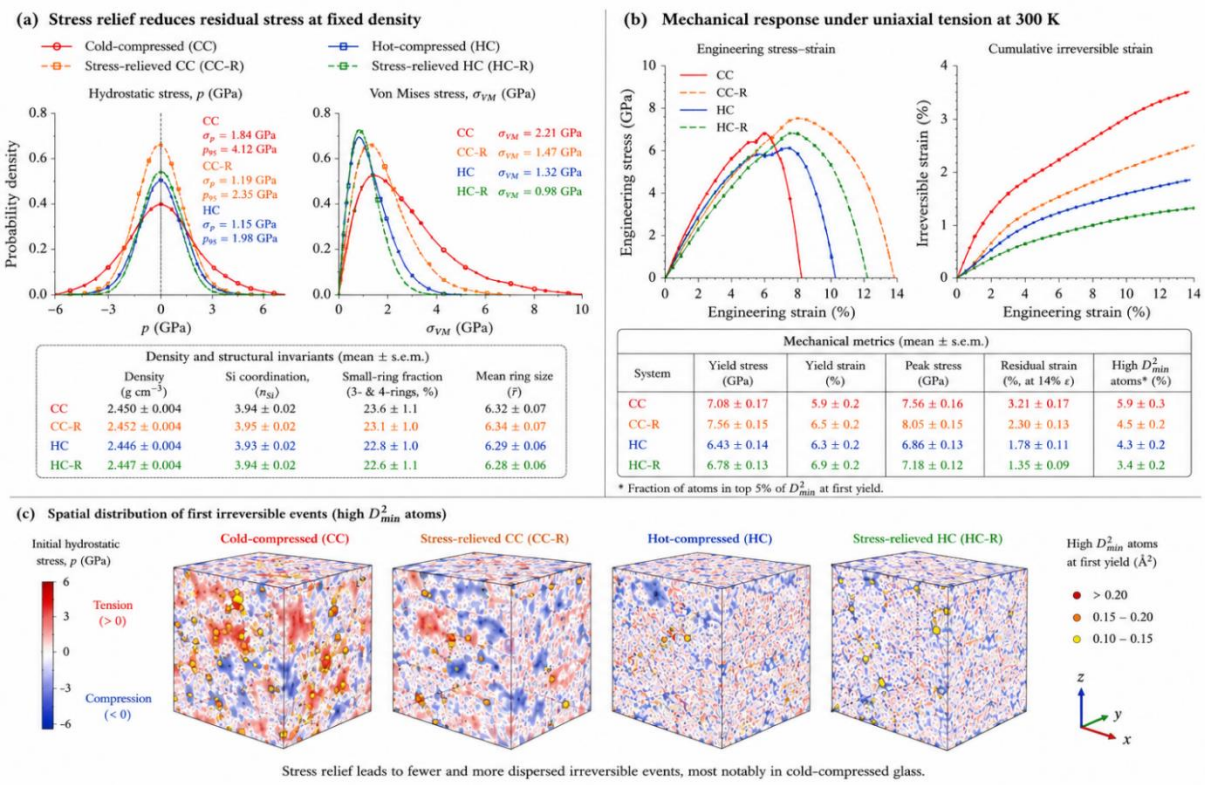

Figure 3: Stress relief enhances the mechanical stability of isodense amorphous SiO_2. (a) Residual hydrostatic and von Mises stress distributions before and after fixed-density stress-relief annealing, showing reduced stress heterogeneity while preserving density and major structural descriptors. (b) Representative stress–strain curves and corresponding mechanical properties, demonstrating increased yield stress and yield strain together with reduced irreversible deformation after stress relief. (c) Spatial distribution of the first irreversible events identified by high D^2_{min} values, showing fewer and more dispersed mechanically active regions following stress relaxation, particularly in the cold-compressed glass.

4.0 CONCLUSION

This study demonstrates that residual internal stress is an independent determinant of the mechanical stability of amorphous SiO_2, even when recovered density is effectively identical. By comparing cold- and hot-compressed glasses prepared from the same parent structures, we showed that a density difference of less than 0.5% masks substantial differences in residual stress heterogeneity. Cold compression retained broader hydrostatic and deviatoric stress distributions together with longer stress-correlation lengths, indicating that processing history leaves a persistent internal stress memory after unloading.

These stress fields were found to directly influence subsequent deformation. Regions with elevated residual tensile stress exhibited a significantly higher probability of non-affine atomic rearrangement and persistent Si–O bond switching during loading. Incorporating residual stress into predictive models substantially improved the identification of mechanically active regions compared with density and structural descriptors alone, demonstrating that local stress provides complementary information beyond medium-range topology. Most importantly, controlled stress-relief annealing reduced stress heterogeneity while preserving density and major structural characteristics, leading to higher yield strength, delayed irreversible deformation, and improved elastic recovery. This causal relationship indicates

that the redistribution of stored elastic energy, rather than changes in network topology, is primarily responsible for the observed enhancement in mechanical stability.
These findings provide direct evidence that residual stress heterogeneity is a preparation-dependent state variable that complements medium-range topology in determining the mechanical response of amorphous SiO_2. The results offer a simple strategy for tailoring the mechanical performance of silica glass through control of internal stress rather than density alone.

REFERENCES

Chen, Y.-C., Lu, Z., Nomura, K., Wang, W., Kalia, R. K., Nakano, A., & Vashishta, P. (2009). Void deformation and breakup in shearing silica glass. *Physical Review Letters, 103*(3), 035501. https://doi.org/10.1103/PhysRevLett.103.035501

Cornet, A., Martinet, C., Martinez, V., & de Ligny, D. (2019). Evidence of polyamorphic transitions during densified SiO_2 glass annealing. *The Journal of Chemical Physics, 151*(16), 164502. https://doi.org/10.1063/1.5121534

Deschamps, T., Margueritat, J., Martinet, C., Mermet, A., & Champagnon, B. (2014). Elastic moduli of permanently densified silica glasses. *Scientific Reports, 4*, 7193. https://doi.org/10.1038/srep07193

Font-Clos, F., Zanchi, M., Homs, A., Matamoros, A., Rountree, C. L., & Barrat, J.-L. (2022). Predicting the failure of two-dimensional silica glasses. *Nature Communications, 13*, 2820. https://doi.org/10.1038/s41467-022-30530-1

Gelin, S., Bonamy, D., Ponson, L., & Bouchaud, E. (2019). Microstructural origin of compressive in situ stresses in amorphous silica thin films. *Physical Review Materials, 3*(5), 055608. https://doi.org/10.1103/PhysRevMaterials.3.055608

Guerette, M., Ackerson, M. R., Thomas, J., Watson, E. B., & Huang, L. (2018). Thermally induced amorphous-to-amorphous transition in hot-compressed silica glass. *The Journal of Chemical Physics, 148*(19), 194501. https://doi.org/10.1063/1.5025592

Guerette, M., Ackerson, M. R., Thomas, J., Yuan, F., Watson, E. B., Walker, D., & Huang, L. (2015). Structure and properties of silica glass densified in cold compression and hot compression. *Scientific Reports, 5*, 15343. https://doi.org/10.1038/srep15343

Hao, T., Marimuthu, K. P., Ravi-Chandar, K., & Kermode, J. R. (2019). Atomistic mechanisms of crack nucleation and propagation in amorphous silica. *Physical Review B, 100*(1), 014204. https://doi.org/10.1103/PhysRevB.100.014204

Huang, L., & Kieffer, J. (2004a). Amorphous–amorphous transitions in silica glass. I. Reversible transitions and thermomechanical anomalies. *Physical Review B, 69*(22), 224203. https://doi.org/10.1103/PhysRevB.69.224203

Huang, L., & Kieffer, J. (2004b). Amorphous–amorphous transitions in silica glass. II. Irreversible transitions and densification limit. *Physical Review B, 69*(22), 224204. https://doi.org/10.1103/PhysRevB.69.224204

Inamura, Y., Katayama, Y., Utsumi, W., & Funakoshi, K. (2004). Transformations in the intermediate-range structure of SiO2 glass under high pressure and temperature. *Physical Review Letters, 93*(1), 015501. https://doi.org/10.1103/PhysRevLett.93.015501

Kobayashi, K., Okumura, M., Nakamura, H., Itakura, M., Machida, M., Urata, S., & Suzuya, K. (2023). Machine learning molecular dynamics reveals the structural origin of the first sharp diffraction peak in high-density silica glasses. *Scientific Reports, 13*, 18721. https://doi.org/10.1038/s41598-023-44732-0

Le, V. V., Nguyen, T. H., & Le, H. M. (2019). Molecular dynamics study of mechanical behavior in silica glass under uniaxial tension. *Computational Materials Science, 159*, 342–352. https://doi.org/10.1016/j.commatsci.2018.12.032

Liang, Y., Miranda, C. R., & Scandolo, S. (2007). Mechanical strength and coordination defects in compressed silica glass: Molecular dynamics simulations. *Physical Review B, 75*(2), 024205. https://doi.org/10.1103/PhysRevB.75.024205

Lunt, A. J. G., Korsunsky, A. M., Baimpas, N., Salvati, E., Sui, T., & Zhang, S. Y. (2018). On the origins of strain inhomogeneity in amorphous materials. *Scientific Reports, 8*, 1574. https://doi.org/10.1038/s41598-018-19900-2

Mantisi, B., Tanguy, A., Kermouche, G., & Barthel, E. (2016). Impact of pressure on plastic yield in amorphous solids with open structure. *Physical Review E, 93*(3), 033001. https://doi.org/10.1103/PhysRevE.93.033001

Martinet, C., Heili, A., Martinez, V., Champagnon, B., Coussa, C., Kermouche, G., Deschamps, T., Margueritat, J., & de Ligny, D. (2015). Permanently densified SiO2 glasses: A structural approach. *Journal of Physics: Condensed Matter, 27*(32), 325401. https://doi.org/10.1088/0953-8984/27/32/325401

Ollier, N., Rygel, J. L., Shcheblanov, N., & Champagnon, B. (2023). Probing densified silica glass structure by molecular dynamics and spectroscopic analysis. *Scientific Reports, 13*, 10292. https://doi.org/10.1038/s41598-023-40270-x

Onodera, Y., Takimoto, Y., Hijiya, H., Taniguchi, T., Urata, S., Fujita, S., Obayashi, I., Nakamura, Y., Hiraoka, Y., & Kohara, S. (2020). Structure and properties of densified silica glass: Characterizing the order within disorder. *NPG Asia Materials, 12*, 85. https://doi.org/10.1038/s41427-020-00262-z

Patinet, S., Vandembroucq, D., & Falk, M. L. (2020). Origin of the Bauschinger effect in amorphous solids. *Physical Review Letters, 124*(20), 205503. https://doi.org/10.1103/PhysRevLett.124.205503

Salmon, P. S., Zeidler A., Shiga, M., Onodera, Y., & Kohara, S. (2023). Ring compaction as a mechanism of densification in amorphous silica. *Physical Review B, 107*(14), 144203. https://doi.org/10.1103/PhysRevB.107.144203

Shiga, M., Hirata, A., Onodera, Y., & Masai, H. (2023). Ring-originated anisotropy of local structural ordering in amorphous and crystalline silicon dioxide. *Communications Materials, 4*, 91. https://doi.org/10.1038/s43246-023-00416-w

Sun, N., Mao, Z., Zhang, X., Tkachev, S. N., & Lin, J.-F. (2022). Hot dense silica glass with ultrahigh elastic moduli. *Scientific Reports, 12*, 13946. https://doi.org/10.1038/s41598-022-18062-6

Yin, S., Li, C., Fang, H., & Ma, Q. (2024). Effects of annealing on thermal stress generation during the cooling process of large-size silica glass. *Journal of Non-Crystalline Solids, 628*, 122804. 10.1016/j.jnoncrysol.2024.122857

Yuan, F., & Huang, L. (2012). Molecular dynamics simulation of amorphous silica under uniaxial tension: From bulk to nanowire. *Journal of Non-Crystalline Solids, 358*(24), 3481–3487. 10.1016/j.jnoncrysol.2012.05.045

Yuan, F., & Huang, L. (2014). Brittle to ductile transition in densified silica glass. *Scientific Reports, 4*, 5035. https://doi.org/10.1038/srep05035

Zanatta, M., Baldi, G., Brusa, R. S., Egger, W., Fontana, A., Gilioli, E., Mariazzi, S., Monaco, G., Ravelli, L., & Sacchetti, F. (2014). Structural evolution and medium-range order in

permanently densified vitreous SiO_2. *Physical Review Letters, 112*(4), 045501. https://doi.org/10.1103/PhysRevLett.112.045501

Zhang, Z., Ispas, S., & Kob, W. (2022). Fracture of silicate glasses: Microcavities and correlations between atomic-scale structure and mechanical response. *Physical Review Materials, 6*(8), 085601. https://doi.org/10.1103/PhysRevMaterials.6.085601